Correlation energies of the high-density spin-polarized electron gas to meV accuracy

Michele Ruggeri, Pablo López Ríos, 1,2 and Ali Alavi 1,3

¹Max Planck Institute for Solid State Research, Heisenbergstr. 1, 70569 Stuttgart, Germany
²Theory of Condensed Matter Group, Cavendish Laboratory, J. J. Thomson Avenue, Cambridge CB3 0HE, UK
³University Chemical Laboratory, Lensfield Road, Cambridge CB2 1EW, UK

We present a novel combination of quantum Monte Carlo methods and a finite size extrapolation framework with which we calculate the thermodynamic limit of the exact correlation energy of the polarized electron gas at high densities to meV accuracy, -40.44(5) and -31.70(4) mHa at $r_{\rm s}=0.5$ and 1, respectively. The fixed-node error is characterized and found to exceed 1 mHa, and we show that the magnitude of the correlation energy of the polarized electron gas is underestimated by up to $6~{\rm meV}$ by the Perdew-Wang parametrization, for which we suggest improvements.

The uniform (or homogeneous) electron gas (UEG) [1] is a system consisting of electrons in a neutralizing uniform background intended to model the behavior of electrons in metals [2]. This system is of crucial importance in understanding the nature of electronic correlation, and is of huge practical relevance since knowledge of the correlation energy of the UEG as a function of its homogeneous density can be used as a key ingredient in the description of the behavior of electrons in real systems [3–5].

Despite its seeming simplicity, the complex correlations caused by the long-ranged character of the Coulomb interaction require the use of explicit many-body methods to accurately characterize the UEG. The release-node diffusion Monte Carlo calculations of Ceperley and Alder (CA) [6] provided data connecting the analytic high-density [7, 8] and low-density [9] limits of the correlation energy, and enabled the development of parametrizations over the entire density range [10–12] which are routinely used in density functional theory calculations.

The Perdew-Wang parametrization of the correlation energy of the UEG (PW92) [12] has become a cornerstone in the construction of density functionals over the past three decades. The PW92 form contains five parameters, of which two are determined from analytic high-density constraints and three by fitting to the CA data. More recently, a "density parameter interpolation" (DPI) parametrization was proposed [13–15] that is constructed by imposing four high-density and three low-density constraints on a seven-parameter functional form, thus requiring (almost) no quantum Monte Carlo input. In Fig. 1 we plot the PW92 and DPI parametrizations for the fully-polarized electron gas, along with the asymptotes defined in Refs. 13–15, as a function of r_s , the radius of the sphere containing one electron on average divided by the Bohr radius. While the two parametrizations are in excellent agreement at low densities, they differ by $\sim 20 \text{ meV}$ at densities relevant to systems with all-electron nuclei [16] and solids at high pressures. The cumulative effect of incurring these small errors in the parametrized correlation energy could result in a significant bias in computed properties, including total and relative energy estimates.

In this Letter we use a combination of full configurationinteraction quantum Monte Carlo (FCIQMC) and fixed-node

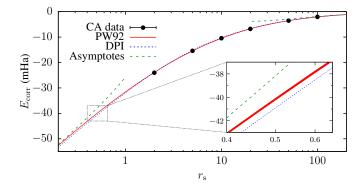


Figure 1. Correlation energy of the polarized UEG as a function of $r_{\rm s}$. Shown are the CA data [6], the PW92 parametrization [12], and the DPI parametrization [13–15]. The inset magnifies the region around $r_{\rm s}=0.5$. The width of the PW92 curve represents its statistical uncertainty.

diffusion Monte Carlo (DMC) to compute the correlation energy of the fully spin-polarized three-dimensional UEG at $r_{\rm s}=0.5$ and 1 to meV accuracy. Building upon existing knowledge of finite size errors in DMC [17–20], we propose an extrapolation procedure which we find to be much more accurate than previous approaches. By extrapolating the fixed node energy and the fixed node error to the thermodynamic limit we obtain the exact correlation energies at $r_{\rm s}=0.5$ and 1. We are thus able to resolve the discrepancy between the values of the PW92 and DPI parametrizations at high densities, and we discuss ways to improve their accuracy.

We simulate finite systems of N same-spin electrons in a cubic simulation cell at fixed homogeneous densities using DMC and FCIQMC. Note that we report energies per electron and use Hartree atomic units ($\hbar=m_e=|e|=4\pi\epsilon_0=1$) throughout. Full details about the methodology and calculations are given in the Supplemental Material [21].

The variational Monte Carlo (VMC) [24–26] and fixed-node DMC methods [6, 27–29] have been extensively used to study the UEG [30–34] using Slater-Jastrow trial wave functions, formed by the Hartree-Fock (HF) determinant multiplied by a Jastrow correlation factor [35, 36], often in combination with backflow transformations [30–32, 37, 38]. While

these wave functions are reasonably sophisticated, the energy obtained by the DMC method incurs a positive bias, referred to as the fixed-node error $\varepsilon_{\rm FN}$, caused by the restrictions imposed by the fixed-node approximation [6, 39].

The FCIQMC method explictly operates in the basis of antisymmetric Slater determinants, thus avoiding the need for a fixed node approximation [40]. The initiator approximation [41] allows the efficient exploration of this vast Hilbert space, and has enabled the successful application of FCIQMC to systems of interest in quantum chemistry and condensed matter physics [42–47], including the unpolarized UEG [48–50, 56]. FCIQMC calculations use finite basis sets, and the infinite basis set limit can be estimated by extrapolation, as is standard practice in quantum chemistry [51]. We find that the basis set error for the polarized UEG is well described by a quadratic function of the inverse basis set size [21], in contrast with the linear dependence found for the unpolarized UEG [48].

We assess the quality of our FCIQMC energies by comparison with VMC and DMC energies for increasingly accurate trial wave functions. We construct multi-determinantal wave functions for the 19-electron gas at $r_{\rm s}=1$ by truncating the FCIQMC wave function to the $N_{\rm d}$ leading determinants, with symmetry-equivalent determinants grouped together. The results, obtained using the CASINO code [52], are plotted in Fig. 2 against $N_{\rm d}$.

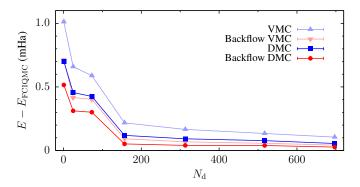


Figure 2. VMC and DMC energies of the polarized 19-electron gas at $r_{\rm s}=1$ (at Γ) relative to FCIQMC, as a function of the number of determinants in the wave function, both without and with backflow transformations.

The variational convergence of our VMC and DMC energies towards the FCIQMC energy is consistent with FCIQMC being exact for this system. The best backflow DMC energy is only 0.027(5) mHa higher than the FCIQMC energy, and is to our knowledge the most accurate DMC energy for this system reported to date.

The finite size error in the energy of the UEG consists of a contribution which varies smoothly with N and a quasirandom contribution, which must be eliminated to enable a clean extrapolation of the smooth part. Twist averaging [17] substantially reduces quasirandom fluctuations by averaging over wave vector offsets in the Brilluoin zone. In DMC we sample the Brillouin zone randomly, while for our FCIQMC calcula-

tions we divide the Brillouin zone into regions of equal total momentum and run FCIQMC calculations in each of these regions [53], which we are able to characterize exactly [21]. In selected cases we perform the basis-set extrapolation in one region and use the extrapolation parameters for the others, which reduces the number of required FCIQMC calculations considerably [21]. In what follows we discuss twist averaged energies except when stated otherwise.

Quasirandom errors are further reduced by subtracting the finite size error in the HF kinetic energy $\Delta K(N) = K(N) - K(\infty)$ from the DMC total energy [6, 19]. Additionally, we find that the residual quasirandom fluctuations are highly correlated with those in the HF exchange energy X(N). The exchange energy is a particularly slowly varying function at large N, so subtracting $X(N) - X(\infty)$ would complicate the extrapolation. However, Drummond $et\ al.$ [19] found that the leading-order contribution to the finite size error in X(N) for an electron gas is exactly $h_2N^{-2/3}$, where $h_2 = -\frac{3\epsilon_1}{16\pi}r_{\rm s}^{-1}$ for the polarized UEG and $\epsilon_1 = 5.674594959$ for simple cubic simulation cells [19, 21]. We therefore obtain the thermodynamic limit by extrapolation of $E_{\rm tot}^{\rm FN}(N) - \Delta K(N) - \Delta X(N)$, where $\Delta X(N) = X(N) - X(\infty) - h_2N^{-2/3}$. This is equivalent to extrapolating $E_{\rm corr}^{\rm FN}(N) + h_2N^{-2/3}$, and in practice we work with the correlation energy directly.

We model the smooth part of the finite size error as a polynomial in $N^{-1/3}$, in agreement with the form of the contributions found by Ref. 19, and we find that the use of the above treatment of quasirandom fluctuations enables the use of fairly high-order polynomials. Chiesa *et al.* [18] showed that the leading-order contribution to the finite size error in the total DMC energy of an electronic system is t_3N^{-1} , where $t_3=-\frac{\sqrt{3}}{2}r_{\rm s}^{-3/2}$ for the polarized UEG. Since beyond-leading-order contributions to both $\Delta K(N)$ and $\Delta X(N)$ are proportional to $N^{-4/3}$ [17, 19], the DMC correlation energy satisfies

$$E_{\text{corr}}^{\text{FN}}(N) + h_2 N^{-2/3} - t_3 N^{-1} = c_0 + c_4 N^{-4/3} + c_5 N^{-5/3} + c_6 N^{-2} + \dots ,$$
 (1)

where $\{c_n\}$ are density-dependent parameters.

We perform DMC calculations of the polarized UEG using the Slater-Jastrow wave function at system sizes $15 \leq N \leq 515$ at $r_{\rm s}=0.5$ and $15 \leq N \leq 1021$ at $r_{\rm s}=1$, and we use Eq. 1 to obtain the thermodynamic limit of the fixed node correlation energy, setting h_2 and t_3 to their analytic values and treating c_0 , c_4 , c_5 , and c_6 as fit parameters. We do not use backflow or multi-determinants to avoid introducing wave function optimization noise in our DMC energies. The magnitude of quasirandom fluctuations has been observed to decay as N^{-1} [17], so we use N^2 as weights in our fits. In Fig. 3 we plot $E_{\rm tot}(N) - \Delta K(N) - \Delta X(N) - t_3 N^{-1}$ and our extrapolation (solid circles and solid line) at $r_{\rm s}=0.5$ as a function of N^{-1} . These results numerically confirm the absence of additional contributions to Eq. 1 at order N^{-1} or slower.

In Fig. 3 we also compare our extrapolation with other approaches used in the literature. Ceperley and Alder [6]

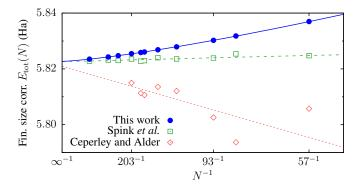


Figure 3. Finite size corrected fixed node energies of the polarized UEG at $r_{\rm s}=0.5$ as a function of N^{-1} . Our results correspond to the solid circles and the solid line. Data replicating the finite size treatment of Ceperley and Alder [6] (open diamonds and dotted line) and Spink *et al.* [34] (open squares) are also plotted, along with an extrapolation of the latter using $N^{-4/3}$ and $N^{-5/3}$ terms.

evaluated $E_{\mathrm{tot},\Gamma}(N) - \Delta K(N)$, where $E_{\mathrm{tot},\Gamma}(N)$ is the total energy at Γ , at closed-shell system sizes in the range $38 \leq N \leq 246$, and used an extrapolation formula including a single N^{-1} term to obtain the thermodynamic limit. A reconstruction of this approach with our DMC data is represented in Fig. 3 (empty diamonds and dotted line); we have used N^2 as weights in the single-term fit. Remarkably, the choice of system sizes is such that the single-term extrapolation yields a nearly identical thermodynamic limit for Γ -point energies as for twist averaged energies, but the absence of higher-order terms in the extrapolation formula results in an underestimation of the total fixed-node energy by about 2 mHa. Higher-order contributions are less important at lower densities, and we conclude that the extrapolation carried out by Ceperley and Alder is very accurate at the densities for which they reported results.

The recent fixed-node DMC study of Spink et al. [34] can be regarded the current state of the art in the treatment of finite size errors. Spink et al. approximate the thermodynamic limit of the total energy by the backflow DMC value of $E_{\rm tot}^{\rm FN}(N)-\Delta K(N)-t_3N^{-1}-T_4N^{-4/3}$ at a single system size, where the last term is the next-to-leading order contribution to the finite size error in the DMC kinetic energy, with $T_4=\frac{\epsilon_3}{16\pi}r_{\rm s}^{-2}$ for the polarized electron gas and $\epsilon_3=21.04959845$ for simple cubic simulation cells [19, 21]. Our reconstruction of this approach using our (non-backflow) DMC data is presented in Fig. 3 (open squares). The quasirandom fluctuations obtained with this approach are small but still significant and, although the data extrapolate to the correct value, individual energy values in Fig. 3 overestimate the thermodynamic limit by up to over 2 mHa. Indeed, the thermodynamic limit of the backflow DMC correlation energy at $r_{\rm s}=0.5$ reported by Spink et al., obtained for a 118-electron system in a face-centred cubic simulation cell, is 2.27(2) mHa above our estimate of the thermodynamic limit of the (nonbackflow) DMC correlation energy.

We turn our attention to the density dependence of Eq. 1, which we re-express as

$$E_{\text{corr}}^{\text{FN}}(\xi) + \tilde{h}_2 \xi^{2/3} - \tilde{t}_3 \xi = c_0 + \tilde{c}_4 \xi^{4/3} + \tilde{c}_5 \xi^{5/3} + \tilde{c}_6 \xi^2 + \dots,$$
(2)

where $\xi=r_{\rm s}^{-3/2}N^{-1}$. We find that assuming tilded coefficients to be density-independent, in line with leading-order extrapolation formulas proposed in the literature [54], incurs a negligible error at high densities. In Fig. 4 we plot $E_{\rm corr}^{\rm FN}(\xi)$ and perform a combined fit of the data at $r_{\rm s}=0.5$ and 1 to Eq. 2, which we find to fit the data very well [21]. We also plot fixed node energies at $r_{\rm s}=5$ to demonstrate the breakdown of this approximation at low densities.

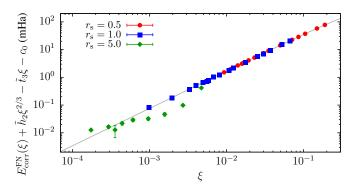


Figure 4. Fixed node correlation energies of the polarized UEG at $r_{\rm s}=0.5,\,1$, and 5 relative to the thermodynamic limit as a function of ξ . The line represents a combined fit of the data at $r_{\rm s}=0.5$ and 1 to Eq. 2, with density-dependent c_0 and density-independent \tilde{c}_4 , \tilde{c}_5 , and \tilde{c}_6 coefficients.

We compute the exact energy of the system using FCIQMC at system sizes N=15, 19, and 27 at $r_{\rm s}=1$ and N=15, 19, 27, and 33 at $r_{\rm s}=0.5$, and we evaluate the fixed node error as the difference between the fixed node and exact correlation energies. We find the fixed node error to increase monotonically with system size [21].

Holzmann *et al.* [20] found that the use of backflow contributes to the finite size error in the energy of the UEG at order N^{-1} . This has the subtle consequence that the coefficient of N^{-1} in the finite size error of the exact energy must differ from t_3 . We assume the fixed node error to have the same asymptotic behavior as the backflow contribution to the energy, which is consistent with the observation of an approximate proportionality between these two quantities [30, 55]. We expect $\varepsilon_{\rm FN}$ to vary less strongly with N than the fixed node energy, and thus we model it using a lower-order expression. Under the assumption that, like $E_{\rm corr}^{\rm FN}$, the exact correlation energy is accurately represented at high densities by a function of ξ , we write

$$\varepsilon_{\text{FN}}(\xi) = f_0 + \tilde{f}_3 \xi + \tilde{f}_4 \xi^{4/3} + \dots ,$$
 (3)

where f_0 is a density-dependent parameter and \tilde{f}_3 and \tilde{f}_4 are density-independent coefficients. We perform a combined fit

of our data at $r_{\rm s}=0.5$ and 1 to Eq. 3 to obtain the thermodynamic limit of the fixed node error at both densities. In Fig. 5 we plot the fixed node error and the resulting fit curves, and in the inset we show the same data as a function of ξ . The results obtained with this procedure are given in Table I and plotted in Fig. 6.

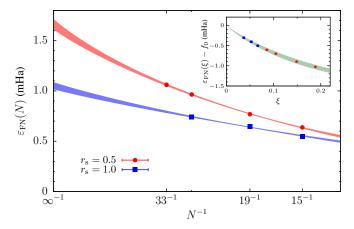


Figure 5. Fixed node error for the polarized UEG at $r_{\rm s}=0.5$ and 1 as a function of N^{-1} . The curves are obtained by simultaneously fitting the data at both densities to Eq. 3 with density-dependent f_0 and density-independent \tilde{f}_3 and \tilde{f}_4 coefficients. The line width represents the statistical uncertainty in the fit. The inset shows the combined fit against ξ .

	$r_{\rm s} = 0.5$	$r_{\rm s} = 1.0$
$E_{\rm corr}^{\rm FN}$	-38.778(10)	-30.650(3)
$\varepsilon_{\mathrm{FN}}$	1.67(5)	1.05(4)
$E_{\rm corr}$	-40.44(5)	-31.70(4)
PW92	-40.2(1)	-31.6(1)
DPI	-40.91	-31.99
uPW92	-40.4(5)	-31.8(4)
rPW92	-40.38(6)	-31.77(8)

Table I. Thermodynamic limit of the fixed node correlation energy, of the fixed node error, and of the exact correlation energy of the polarized UEG at $r_{\rm s}=0.5$ and 1, in mHa. Also shown are values of the PW92 and DPI parametrizations, an unweighted PW92 fit to the CA data (uPW92), and a revised unweighted PW92 fit to the CA data and our results (rPW92).

Before comparing our results with existing parametrizations, we note two problematic aspects of the PW92 fit. First, the statistical uncertainty of the CA data propagates to the parametrized correlation energies, which thus incur a random bias of magnitude proportional to the uncertainty, but this was ignored after fitting. We have calculated these propagated uncertainties, shown in Table I and Fig. 6. Second, the CA data were weighted by their inverse square uncertainty in the PW92 fit (a "chi-square" fit), but these span over two orders of magnitude, and in effect the PW92 parametrization ignores the

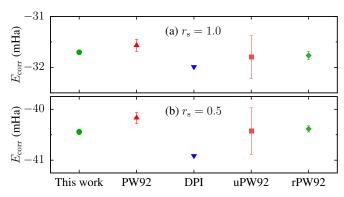


Figure 6. Correlation energy of the polarized UEG at (a) $r_{\rm s}=1$ and (b) $r_{\rm s}=0.5$ from our caculations, and values of the PW92 and DPI parametrizations, our unweighted PW92 fit to the CA data (uPW92), and our revised unweighted PW92 fit to the CA data and our present results (rPW92).

CA data for $r_{\rm s} \leq 10$: fitting the CA energies for $r_{\rm s} = 20, 50,$ and 100 to the PW92 form gives essentially identical results to the "chi-square" fit using all the data. In Table I and Fig. 6 we report values of an unweighted PW92 fit to the CA data (uPW92) and of an unweighted PW92 fit to the CA data and our present results (rPW92).

We find that the magnitude of the correlation energy is underestimated by the PW92 parametrization by about 3–6 meV, and overestimated by the DPI parametrization by 8–13 meV. The correlation energies obtained from the unweighted uPW92 fit have rather large uncertainties, but their expected values are more accurate than those from the weighted fit. Our revised rPW92 fit delivers the correct correlation energies at both densities with negligible bias and a factor of 5–10 smaller uncertainties than the uPW92 fit.

By construction, the accuracy of the DPI parameterization at finite densities depends exclusively on its functional form. Modifications to include more high-density constraints would be advisable in order to enable better agreement with our results. Alternatively, additional degrees of freedom could be used to fit parameters to quantum Monte Carlo data, which would be advantageous over our rPW92 fit since the DPI form has the correct analytic structure in the high- and low-density limits [13].

The authors would like to thank H. Luo, J.J. Shepherd, R.J. Needs, and M. Holzmann for useful discussions. Financial support and computational resources have been provided by the Max-Planck-Gesellschaft.

^[1] P.-F. Loos and P. M. W. Gill, *The uniform electron gas*, Wiley Interdiscip. Rev. Comput. Mol. Sci. **6**, 410 (2016).

^[2] S. Huotari, J. A. Soinienm, T. Pylkännen, K. Hämäläinen, A. Issolah, A. Titov, J. McMinis, J. Kim, K. Esler, D. M. Ceperley, M. Holzmann, and V. Olevano, *Momentum Distribution and Renormalization Factor in Sodium and the Electron Gas*,

- Phys. Rev. Lett. 105, 086403 (2010).
- [3] E. Wigner, Effects of the electron interaction on the energy levels of electrons in metals, Trans. Faraday Soc. 34, 678 (1938).
- [4] P. Hohenberg and W. Kohn, *Inhomogeneous Electron Gas*, Phys. Rev. 136, B864 (1964).
- [5] W. Kohn and L. J. Sham, Self-Consistent Equations Including Exchange and Correlation Effects, Phys. Rev. 140, A1133 (1965).
- [6] D. M. Ceperley and B. J. Alder, *Ground State of the Electron Gas by a Stochastic Method*, Phys. Rev. Lett. **45**, 566 (1980).
- [7] M. Gell-Mann and K. A. Brueckner, *Correlation Energy of an Electron Gas at High Density*, Phys. Rev. **106**, 364 (1957).
- [8] G. G. Hoffman, Correlation energy of a spin-polarized electron gas at high density, Phys. Rev. B 45, 8730 (1992).
- [9] W. J. Carr, Jr., Energy, Specific Heat, and Magnetic Properties of the Low-Density Electron Gas, Phys. Rev. 122, 1437 (1961).
- [10] S. H. Vosko, L. Wilk, M. Nusair, Accurate spin-dependent electron liquid correlation energies for local spin density calculations: a critical analysis, Can. J. Phys. 58, 1200 (1980).
- [11] J. P. Perdew and A. Zunger, Self-interaction correction to density-functional approximations for many-electron systems, Phys. Rev. B 23, 5048 (1981).
- [12] J. P. Perdew, Y. Wang, Accurate and simple analytic representation of the electron-gas correlation energy, Phys. Rev. B **45**, 13244 (1992).
- [13] J. Sun, J. P. Perdew, and M. Seidl, Correlation energy of the uniform electron gas from an interpolation between high- and low-density limits, Phys. Rev. B 81, 085123 (2010).
- [14] P.-F. Loos and P. M. W. Gill, Correlation energy of the spin-polarized uniform electron gas at high density, Phys. Rev. B 84, 033103 (2011).
- [15] P. Bhattarai, A. Patra, C. Shahi, and J. P. Perdew, *How accurate are the parametrized correlation energies of the uniform electron gas?*, Phys. Rev. B **97**, 195128 (2018).
- [16] A. Zupan, K. Burke, M. Ernzerhof, and J. P. Perdew, Distributions and averages of electron density parameters: Explaining the effects of gradient corrections, J. Chem. Phys. 106, 10184 (1997).
- [17] C. Lin, F. H. Zong, and D. M. Ceperley, Twist-averaged boundary conditions in continuum quantum Monte Carlo algorithms, Phys. Rev. E 64, 016702 (2001).
- [18] S. Chiesa, D. M. Ceperley, R. M. Martin, and M. Holzmann, Finite-Size Error in Many-Body Simulations with Long-Range Interactions, Phys. Rev. Lett. 97, 076404 (2006).
- [19] N. D. Drummond, R. J. Needs, A. Sorouri, and W. M. C. Foulkes, Finite-size errors in continuum quantum Monte Carlo calculations, Phys. Rev. B 78, 125106 (2008).
- [20] M. Holzmann, R. C. Clay, III, M. A. Morales, N. M. Tubman, D. M. Ceperley, and C. Pierleoni, *Theory of finite size effects for electronic quantum Monte Carlo calculations of liquids and solids*, Phys. Rev. B 94, 035126 (2016).
- [21] See the Supplemental Material at [URL] for details of the system and methodology, including twist averaging, Brillouin zone division, trial wave functions, finite size errors, and additional results. The Supplemental Material cites Refs. 22 and 23.
- [22] P. P. Ewald, Die Berechnung optischer und elektrostatischer Gitterpotentiale, Ann. Phys. 64, 253 (1921).
- [23] T. Kato, On the eigenfunctions of many-particle systems in quantum mechanics, Comm. Pure Appl. Math. 10, 151 (1957).
- [24] W. L. McMillan, Ground State of Liquid He⁴, Phys. Rev. 138, A442 (1965).
- [25] J. Toulouse and C. J. Umrigar, Optimization of quantum Monte Carlo wave functions by energy minimization, J. Chem. Phys. 126, 084102 (2007).

- [26] C. J. Umrigar, J. Toulouse, C. Filippi, S. Sorella, and R. G. Hennig, Alleviation of the Fermion-Sign Problem by Optimization of Many-Body Wave Functions, Phys. Rev. Lett. 98, 110201 (2007).
- [27] W. M. C. Foulkes, L. Mitas, R. J. Needs, and G. Rajagopal, *Quantum Monte Carlo simulations of solids*, Rev. Mod. Phys. 73, 33 (2001).
- [28] C. J. Umrigar, M. P. Nightingale, and K. J. Runge, A diffusion Monte Carlo algorithm with very small time-step errors, J. Chem. Phys. 99, 2865 (1993).
- [29] A. Zen, S. Sorella, M. J. Gillan, A. Michaelides, and D. Alfè, Boosting the accuracy and speed of quantum Monte Carlo: Size consistency and time step, Phys. Rev. B 93, 241118(R) (2016).
- [30] Y. Kwon, D. M. Ceperley, and R. M. Martin, Effects of backflow correlation in the three-dimensional electron gas: Quantum Monte Carlo study, Phys. Rev. B 58, 6800 (1998).
- [31] M. Holzmann, D. M. Ceperley, C. Pierleoni, and K. Esler, *Backflow correlations for the electron gas and metallic hydrogen*, Phys. Rev. E **68**, 046707 (2003).
- [32] P. López Ríos, A. Ma, N. D. Drummond, M. D. Towler, and R. J. Needs, *Inhomogeneous backflow transformations in quantum Monte Carlo calculations*, Phys. Rev. E 74, 066701 (2006).
- [33] I. G. Gurtubay, R. Gaudoin, and J. M. Pitarke, Benchmark quantum Monte Carlo calculations of the ground-state kinetic, interaction and total energy of the three-dimensional electron gas, J. Phys.: Condens. Matter 22, 065501 (2010).
- [34] G. G. Spink, N. D. Drummond, and R. J. Needs Quantum Monte Carlo study of the three-dimensional spin-polarized homogeneous electron gas, Phys. Rev. B 88, 085121 (2013).
- [35] N. D. Drummond, M. D. Towler, and R. J. Needs, Jastrow correlation factor for atoms, molecules, and solids, Phys. Rev. B 70, 235119 (2004).
- [36] P. López Ríos, P. Seth, N. D. Drummond, and R. J. Needs, Framework for constructing generic Jastrow correlation factors, Phys. Rev. E 86, 036703 (2012).
- [37] V. R. Pandharipande and N. Itoh, Effective Mass of ³He in Liquid ⁴He, Phys. Rev. A 8, 2564 (1973).
- [38] K. E. Schmidt and V. R. Pandharipande, New variational wave function for liquid ³He, Phys. Rev. B 19, 2504 (1979).
- [39] J. B. Anderson, *Quantum chemistry by random walk*. $H^{-2}P$, H_3^+ $D_{3h}^{-1}A_1'$, $H_2^ 3\Sigma_u^+$, $H_4^{-1}\Sigma_g^+$, $Be^{-1}S$, J. Chem. Phys. **65**, 4121 (1976).
- [40] G. H. Booth, A. J. W. Thom, and A. Alavi, Fermion Monte Carlo without fixed nodes: A game of life, death, and annihilation in Slater determinant space, J. Chem. Phys. 131, 054106 (2009).
- [41] D. Cleland, G. H. Booth, and A. Alavi, Survival of the fittest: Accelerating convergence in full configuration-interaction quantum Monte Carlo, J. Chem. Phys. 132, 041103 (2010).
- [42] D. Cleland, G. H. Booth, C. Overy, and A. Alavi, Taming the First-Row Diatomics: A Full Configuration Interaction Quantum Monte Carlo Study, J. Chem. Theory Comput. 8, 4138 (2012).
- [43] J. A. F. Kersten, G. H. Booth and A. Alavi, Assessment of multireference approaches to explicitly correlated full configuration interaction quantum Monte Carlo, J. Chem. Phys. 145, 054117 (2016).
- [44] L. R. Schwarz, G. H. Booth and A. Alavi, *Insights into the structure of many-electron wave functions of Mottinsulating antiferromagnets: The three-band Hubbard model in full configuration interaction quantum Monte Carlo*, Phys. Rev. B **91**, 045139 (2015).
- [45] G. H. Booth and A. Alavi, Approaching chemical accuracy using full configuration-interaction quan-

- tum Monte Carlo: A study of ionization potentials, J. Chem. Phys. **132**, 174104 (2010).
- [46] D. Cleland, G. H. Booth, and A. Alavi, A study of electron affinities using the initiator approach to full configuration interaction quantum Monte Carlo, J. Chem. Phys. 134, 024112 (2011).
- [47] G. H. Booth, D. Cleland, A. J. W. Thom, and A. Alavi, *Breaking the carbon dimer: The challenges of multiple bond dissociation with full configuration interaction quantum Monte Carlo methods*, J. Chem. Phys. **135**, 084104 (2011).
- [48] J. J. Shepherd, G. H. Booth, and A. Alavi, Investigation of the full configuration interaction quantum Monte Carlo method using homogeneous electron gas models, J. Chem. Phys. 136, 244101 (2012).
- [49] J. J. Shepherd, G. H. Booth, A. Grüneis, and A. Alavi, Full configuration interaction perspective on the homogeneous electron gas, Phys. Rev. B 85, 081103(R) (2012).
- [50] H. Luo and A. Alavi, Combining the Transcorrelated Method with Full Configuration Interaction Quantum Monte

- Carlo: Application to the Homogeneous Electron Gas, J. Chem. Theory Comput. 14, 1403 (2018).
- [51] T. Helgaker, P. Jørgensen, and J. Olsen, Molecular Electronic-Structure Theory (Wiley, Chichester, 2000).
- [52] R. J. Needs, M. D. Towler, N. D. Drummond, and P. López Ríos, Continuum variational and diffusion quantum Monte Carlo calculations, J. Phys.: Condens. Matter 22, 023201 (2010).
- [53] J. J. Shepherd, A quantum chemical perspective on the homogeneous electron gas, PhD thesis, University of Cambridge (2013).
- [54] D. M. Ceperley, Ground state of the fermion one-component plasma: A Monte Carlo study in two and three dimensions, Phys. Rev. B 18, 3126 (1978).
- [55] P. Seth, P. López Ríos, and R. J. Needs, Quantum Monte Carlo study of the first-row atoms and ions, J. Chem. Phys. 134, 084105 (2011).
- [56] V. A. Neufeld and A. J. W. Thom, A study of the dense uniform electron gas with high orders of coupled cluster, J. Chem. Phys. 147, 194105 (2017).

Correlation energies of the high-density spin-polarized electron gas to meV accuracy: Supplemental Material

THE UNIFORM ELECTRON GAS

The first-quantized Hamiltonian of the infinite UEG is, in Hartree atomic units ($\hbar=m_e=|e|=4\pi\epsilon_0=1$),

$$\hat{H} = -\frac{1}{2} \sum_{i} \nabla_i^2 + \sum_{i < j} \frac{1}{|\mathbf{r}_i - \mathbf{r}_j|}, \qquad (S1)$$

where ${\bf r}_i$ is the position vector of the ith electron, and the system is characterized by its uniform number density n, usually specified via $r_{\rm s}=(4\pi n/3)^{-1/3}$. The second-quantized Hamiltonian of the infinite UEG is

$$\hat{H} = \frac{1}{2} \sum_{\mathbf{k}} k^2 a_{\mathbf{k}}^{\dagger} a_{\mathbf{k}} + \sum_{\mathbf{p}, \mathbf{q}} \sum_{\mathbf{k} \neq \mathbf{0}} \frac{4\pi}{k^2} a_{\mathbf{p}+\mathbf{k}}^{\dagger} a_{\mathbf{q}-\mathbf{k}}^{\dagger} a_{\mathbf{q}} a_{\mathbf{p}} , \quad (S2)$$

where \mathbf{k} , \mathbf{p} , and \mathbf{q} are reciprocal-space vectors, and $a_{\mathbf{k}}^{\dagger}$ and $a_{\mathbf{k}}$ are the creation and annihilation operators for the single-electron state of wave vector \mathbf{k} , respectively. The Fermi wave vector, $k_{\mathrm{F}} = (6\pi^2 n)^{1/3}$ at full spin polarization, characterizes the system. The kinetic energy term is diagonal, and the interaction term only connects states with equal total momentum \mathbf{k}_{T} . The Hilbert space of the system thus consists of disjoint subspaces corresponding to different \mathbf{k}_{T} , and the ground state is the solution of the Schrödinger equation in the subspace for which the total energy is minimized.

We simulate a finite version of this system consisting of N electrons in a cubic simulation cell of side $L=(n/N)^{1/3}$ subject to periodic boundary conditions. This requires replacing the Coulomb interaction in Eq. S1 with an Ewald summation [S1], restricting the summations in Eq. S2 to reciprocal lattice vectors, $\mathbf{G} = \frac{2\pi}{L}(i_x,i_y,i_z)$, where i_x,i_y , and i_z are integers, and adding a self-interaction constant to both Hamiltonians.

In the high density regime the UEG behaves as a Fermi liquid, for which a plane-wave basis is a natural choice. The configuration interaction (CI) expansion of the ground-state wave function is $\Psi_0 = \sum_I C_I D_I$, where $\{C_I\}$ are the CI coefficients, $D_I = \det(e^{i\mathbf{G}_{\mu_{Ij}}\cdot\mathbf{r}_i})$ are determinants of plane-wave orbitals, and μ_{Ij} is the index of the jth wave vector occupied in the Ith determinant. We label the HF determinant, which corresponds to the choice of I that minimizes $\langle D_I|\hat{H}|D_I\rangle/\langle D_I|D_I\rangle$, as I=1.

TWIST AVERAGING

The translational invariance of the wave function of a periodic system is defined up to a phase factor, $\Psi(\mathbf{r}_1,...,\mathbf{r}_i+\mathbf{R},...,\mathbf{r}_N)=e^{i\theta}\Psi(\mathbf{r}_1,...,\mathbf{r}_i,...,\mathbf{r}_N)$, where \mathbf{R} is a simulation cell lattice vector, $\mathbf{R}=L(i_x,i_y,i_z)$, and i_x,i_y , and i_z are integers. This phase factor can be obtained by shifting the reciprocal lattice by a certain \mathbf{k}_s in the Brillouin zone such that $\theta=\mathbf{k}_s\cdot\mathbf{R}$.

We note that the total momentum $\mathbf{k}_{\mathrm{T}} = \sum_{i} \mathbf{G}_{\mu_{1i}}$ of the ground-state wave function changes discretely with \mathbf{k}_{s} , dividing the Brillouin zone into Z regions associated with different \mathbf{k}_{T} . Since it is not trivial to determine *a priori* which \mathbf{k}_{T} yields the lowest energy at a given \mathbf{k}_{s} , \mathbf{k}_{T} is usually chosen so as to minimize the energy of the non-interacting system, resulting in convex polyhedral regions bounded by Bragg planes [S2].

Averaging an expectation value A over \mathbf{k}_s in the Brillouin zone,

$$A_{\rm TA} = \frac{1}{\Omega_{\rm BZ}} \int_{\rm BZ} A(\mathbf{k}_{\rm s}) \, \mathrm{d}\mathbf{k}_{\rm s} \,, \tag{S3}$$

where Ω_{BZ} is the volume of the Brillouin zone, is referred to as twist averaging, and has the effect of reducing quasirandom fluctuations of the expectation value with system size N [S2]. The integration over \mathbf{k}_s is usually performed stochastically or using a grid in the Brillouin zone [S2, S3]. However, inspection of the second-quantized Hamiltonian of Eq. S2 reveals that, for a fixed \mathbf{k}_T , shifting the reciprocal lattice by \mathbf{k}_s adds a constant to the diagonal kinetic energy term and leaves the interaction term unchanged, since it only depends on differences between reciprocal lattice vectors. Therefore the correlation energy only depends on the total momentum \mathbf{k}_T , which changes discretely with \mathbf{k}_s , and therefore the integral reduces to a sum over the Z regions in which the total momentum is constant,

$$E_{\text{corr}}^{\text{TA}} = \frac{1}{\Omega_{\text{BZ}}} \int_{\text{BZ}} E_{\text{corr}}(\mathbf{k}_{\text{s}}) d\mathbf{k}_{\text{s}}$$
$$= \sum_{z} \frac{\Omega_{z}}{\Omega_{\text{BZ}}} E_{\text{corr}}(\mathbf{k}_{\text{s}}^{z}) ,$$
 (S4)

where Ω_z is the volume of the zth region and $\mathbf{k}_{\mathrm{s}}^z$ is an arbitrary reciprocal lattice shift in the zth region.

This suggests a twist-averaging scheme which is more efficient than other approaches at small system sizes [S4]. By expressing the total energy as the HF energy plus the correlation energy, $E_{\rm tot}({\bf k}_{\rm s}) = E_{\rm HF}({\bf k}_{\rm s}) + E_{\rm corr}({\bf k}_{\rm s})$, the HF energy absorbs the continuous variation of the kinetic energy with ${\bf k}_{\rm s}$, while the correlation energy is constant within each region. Evaluating the average correlation energy weighted by the region volumes, which can be obtained exactly for $N \lesssim 100$, see below, yields the twist-averaged correlation energy. We use this scheme to twist-average our FCIQMC energies, and we use random sampling to twist-average our DMC energies.

Exact division of the Brillouin zone

The energy (per electron) of the non-interacting electron gas equals the HF kinetic energy,

$$E_{\rm NI}(\mathbf{k}_{\rm s}; \mathbf{k}_{\rm T}) = K_{1}(\mathbf{k}_{\rm s}; \mathbf{k}_{\rm T})$$

$$= \frac{1}{2N} \sum_{i=1}^{N} (\mathbf{G}_{\mu_{1i}} + \mathbf{k}_{\rm s})^{2}$$

$$= \frac{1}{2N} \sum_{i=1}^{N} (G_{\mu_{1i}}^{2} + k_{\rm s}^{2} + 2\mathbf{G}_{\mu_{1i}} \cdot \mathbf{k}_{\rm s})$$

$$= E_{\rm NI}(\mathbf{0}; \mathbf{k}_{\rm T}) + \frac{1}{2}k_{\rm s}^{2} + \frac{1}{N}\mathbf{k}_{\rm T} \cdot \mathbf{k}_{\rm s},$$
(S5)

where $\{\mu_{1i}\}$ are the indices of the reciprocal lattice vectors occupied in the HF determinant. These indices determine \mathbf{k}_{T} and *vice versa*. The energy of the non-interacting system at fixed \mathbf{k}_{T} is a paraboloid centred at $\mathbf{k}_{\mathrm{s}} = -\frac{1}{N}\mathbf{k}_{\mathrm{T}}$. Since the total momentum at shift \mathbf{k}_{s} is that which minimizes $E_{\mathrm{NI}}(\mathbf{k}_{\mathrm{s}};\mathbf{k}_{\mathrm{T}})$, \mathbf{k}_{T} changes discretely at the intersection of two such paraboloids. If $\mathbf{k}_{\mathrm{T}}^{z_1}$ and $\mathbf{k}_{\mathrm{T}}^{z_2}$ are the total momenta of two adjacent regions, this intersection is given by

$$\frac{1}{N} \left(\mathbf{k}_{\mathrm{T}}^{z_{1}} - \mathbf{k}_{\mathrm{T}}^{z_{2}} \right) \cdot \mathbf{k}_{\mathrm{s}} = E_{\mathrm{NI}}(\mathbf{0}; \mathbf{k}_{\mathrm{T}}^{z_{2}}) - E_{\mathrm{NI}}(\mathbf{0}; \mathbf{k}_{\mathrm{T}}^{z_{1}}) , \quad (86)$$

which is the equation of a plane. The Brillouin zone regions of constant total momentum are therefore convex polyhedra.

In practice we work in the irreducible Brullouin zone (IBZ), which for a simple cubic simulation cell is the tetrahedron given by $0 \le z \le y \le x \le \pi/L$, where x, y, and z are the Cartesian components of \mathbf{k}_{s} . Consequently the total momentum $\mathbf{k}_{\mathrm{T}} = \frac{\pi}{L}(i_x, i_y, i_z)$, where i_x, i_y , and i_z are integers, satisfies $0 \le -i_z \le -i_y \le -i_x \le N/2$.

The problem of dividing the IBZ reduces to locating the vertices of the polyhedral regions. Note that Eq. S6 represents a Bragg plane, which can be defined in terms of integers, and the region vertices are the intersections of three or more interregion and/or IBZ planes, and are therefore proportional to vectors of rational numbers. The use of integer arithmetic enables solving the IBZ division problem exactly for moderate system sizes.

Given a shift \mathbf{k}_s , finding the N reciprocal lattice vectors with the smallest $|\mathbf{G}_j + \mathbf{k}_s|$ yields the indices of the occupied orbitals $\{\mu_{1i}\}$, which determines \mathbf{k}_T . However, at points on inter-region planes the set of occupied orbitals is not unique, and multiple total momenta give the same, degenerate kinetic energy. The allowed values of the total momentum at a vertex can be obtained by considering all possible occupations, and the equations of the inter-region planes passing through the vertex are given by Eq. S6 for each pair of allowed total momenta. In turn, each pair of planes intersect at a line corresponding to a polyhedral edge which points to an adjacent vertex.

It is thus possible to find the vertices of all polyhedral regions in the IBZ by successively moving between adjacent

vertices along region edges. We illustrate our algorithm using the particularly simple case of the 7-electron gas, which we do not consider in our main results. The IBZ division for this example is shown in Fig. S1, where we have labelled the high-symmetry points Γ , X, M, and R at the corners of the IBZ and the additional vertices α , β , γ , δ , and ε .

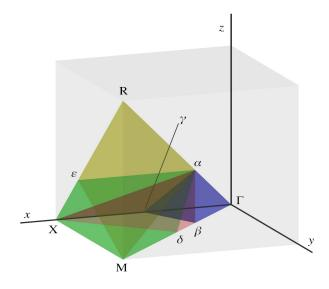


Figure S1. Division of the IBZ of the 7-electron gas into regions of constant total momentum.

We start at Γ , where we find that $\mathbf{k}_T=\mathbf{0}$ is the only allowed value of the total momentum. We then perform a line search between Γ and \mathbf{M} , corresponding to the intersection between two of the three IBZ planes passing through Γ , to find the point furthest from Γ at which *any* of the allowed values of the total momentum at Γ is also an allowed value. This is done by bisection using floating-point arithmetic, and upon locating vertex $\beta = \frac{2\pi}{L}(\frac{1}{6},\frac{1}{6},0)$ we revert to using integer arithmetic. Inspecting the degenerate occupations at β yields two possible total momenta, $\mathbf{k}_T=\mathbf{0}$ and $-\frac{2\pi}{L}(2,1,0)$, defining an interregion plane of normal (2,1,0). The pairwise intersections between this plane and the two IBZ planes passing through β provide search directions to find adjacent vertices α , γ , and δ , and this process continues until we exhaust the lists of edges radiating from all vertices.

The resulting vertex locations characterize the regions and, using the divergence theorem, we obtain their volume, center, and contributions to the HF kinetic energy (the HF exchange energy is constant within each region). For instance, the twist-averaged kinetic and exchange energy of the 7-electron gas are exactly

$$K = \frac{215}{504} \left(\frac{6\pi^2}{7}\right)^{2/3} r_{\rm s}^{-2} , \qquad (S7)$$

and

$$X = -\frac{7459}{3780} \left(\frac{3}{28\pi^4}\right)^{1/3} r_{\rm s}^{-1} + v_{\rm M} r_{\rm s}^{-1} , \qquad (S8)$$

where $v_{\rm M}=-0.46005809$ is the self-image energy contribution for this system at $r_{\rm s}=1$. These integrals can also be carried out accurately using floating-point arithmetic; the use of integers is however crucial for the location of vertices, since for $N\gtrsim 30$ the proximity of some of the vertices can cause incorrect IBZ division under floating-point arithmetic.

In Tables S1, S2, and S3 we give the exact region volumes and centers (the latter truncated to four decimals for conciseness) of the IBZ regions corresponding to $N=15,\,19,\,27,\,19,\,27,\,19$, and 33, for which we have run FCIQMC calculations, as well as those for the 7-electron system of Fig. S1. In Fig. S2 we plot the number of regions Z as a function of N, showing that $Z\sim N^2$. Therefore the number of evaluations of an expectation value required for twist averaging increases quadratically with system size.

N	z	$-\frac{L}{2\pi}\mathbf{k}_{\mathrm{T}}^{z}$	$\Omega_z/\Omega_{ m BZ}$	$rac{L}{2\pi}\mathbf{k}_{\mathrm{s}}^{z}$
7	0	(0, 0, 0)	1/18	(0.1458, 0.0833, 0.0417)
	1	(2, 1, 0)	1/9	(0.2708, 0.1146, 0.0417)
	2	(3, 2, 1)	7/18	(0.3899, 0.2173, 0.0655)
	3	(3, 3, 3)	4/9	(0.4167, 0.3333, 0.2083)
15	0	(3, 2, 1)	13/252	(0.1513, 0.1036, 0.0499)
	1	(4, 0, 0)	1/28	(0.2411, 0.0491, 0.0179)
	2	(5, 2, 2)	4/21	(0.3452, 0.1845, 0.1533)
	3	(4, 4, 1)	7/72	(0.2798, 0.2485, 0.1488)
	4	(6, 4, 0)	5/8	(0.4250, 0.2937, 0.1250)
19	0	(0, 0, 0)	1/40	(0.1188, 0.0562, 0.0250)
	1	(2, 2, 1)	11/360	(0.1680, 0.1055, 0.0553)
	2	(4, 3, 1)	1/7	(0.2606, 0.1728, 0.0558)
	3	(6, 2, 1)	83/2520	(0.3354, 0.1143, 0.0497)
	4	(5, 3, 3)	19/105	(0.3392, 0.2646, 0.2079)
	5	(6, 4, 2)	4/55	(0.3856, 0.3391, 0.1614)
	6	(7, 3, 0)	205/5544	(0.3920, 0.2406, 0.0216)
	7	(8,0,0)	1/56	(0.3705, 0.0491, 0.0179)
	8	(8, 3, 2)	146/693	(0.4487, 0.2780, 0.1765)
	9	(9, 1, 1)	43/504	(0.4479, 0.1271, 0.0540)
	10	(7, 6, 1)	19/792	(0.4098, 0.3794, 0.1298)
	11	(9, 5, 1)	17/396	(0.4711, 0.3528, 0.1290)
	12	(9, 8, 0)	7/72	(0.4658, 0.4211, 0.1250)

Table S1. Index z, total momentum $\mathbf{k}_{\mathrm{T}}^{z}$, exact weight $\Omega_{z}/\Omega_{\mathrm{BZ}}$, and center $\mathbf{k}_{\mathrm{s}}^{z}$ of the IBZ regions for N=7,15, and 19.

The need to enumerate all possible occupations of partially-filled shells causes a computational bottleneck in our exact division algorithm, which we are able to use in practice for $N \lesssim 100$. Computing twist-averaged DMC correlation energies requires knowledge of the corresponding twist-averaged HF energy components, which we obtain using random sampling for $N \gtrsim 100$. Our twist-averaged HF energies are given in Table S4.

N	z	$-rac{L}{2\pi}\mathbf{k}_{\mathrm{T}}^{z}$	$\Omega_z/\Omega_{ m BZ}$	$rac{L}{2\pi}\mathbf{k}_{\mathrm{s}}^{z}$
27	0	(0,0,0)	1/60	(0.0979, 0.0563, 0.0250)
	1	(3, 1, 1)	2/35	(0.2009, 0.0828, 0.0493)
	2	(4, 4, 0)	2363/18900	(0.2514, 0.1808, 0.0633)
	3	(5, 3, 3)	26/945	(0.2706, 0.2041, 0.1763)
	4	(6, 3, 0)	1/84	(0.3235, 0.0908, 0.0250)
	5	(7, 4, 1)	1409/17160	(0.3423, 0.2085, 0.0910)
	6	(6, 5, 4)	34/2925	(0.3055, 0.2652, 0.2258)
	7	(7, 6, 0)	1/200	(0.3271, 0.2889, 0.0250)
	8	(9, 2, 2)	16/315	(0.3851, 0.1327, 0.0968)
	9	(7, 7, 2)	2/585	(0.3143, 0.2951, 0.1647)
	10	(9, 5, 0)	1/840	(0.4051, 0.2286, 0.0114)
	11	(10, 3, 1)	299/18480	(0.4258, 0.1805, 0.0586)
	12	(10, 5, 2)	1732/69615	(0.4111, 0.2256, 0.1476)
	13	(9, 7, 1)	1009/10296	(0.3923, 0.3282, 0.0672)
	14	(9, 6, 5)	33/7735	(0.3493, 0.2623, 0.2338)
	15	(8, 8, 4)	298/47775	(0.3307, 0.3078, 0.2195)
	16	(12, 1, 0)	1/16	(0.4485, 0.1013, 0.0417)
	17	(11, 5, 5)	11/1428	(0.4264, 0.2296, 0.2149)
	18	(10, 8, 3)	2458/97461	(0.3989, 0.3563, 0.1501)
	19	(12, 6, 1)	62/1001	(0.4670, 0.2841, 0.0559)
	20	(13, 4, 0)	5/504	(0.4790, 0.1963, 0.0417)
	21	(12, 7, 3)	145/1989	(0.4609, 0.3058, 0.1475)
:	22	(11, 8, 6)	8413/324870	(0.3955, 0.2993, 0.2390)
	23	(11, 10, 5)	23/3185	(0.4239, 0.3977, 0.1563)
	24	(13, 9, 5)	10/637	(0.4754, 0.3651, 0.1677)
	25	(12, 9, 9)	1/30	(0.4292, 0.3458, 0.3250)
	26	(11, 11, 8)	5/147	(0.4066, 0.3829, 0.3036)
	27	(13, 10, 8)	19/588	(0.4745, 0.3639, 0.2979)
	28	(13, 12, 7)	17/245	(0.4718, 0.4330, 0.2307)

Table S2. Index z, total momentum ${\bf k}_{\rm T}^z$, exact weight $\Omega_z/\Omega_{\rm BZ}$, and center ${\bf k}_{\rm s}^z$ of the IBZ regions for N=27.

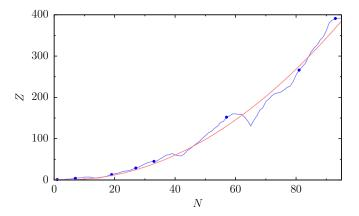


Figure S2. Number of IBZ regions as a function of system size for simple cubic simulation cells. The circles correspond to closed shell systems, and the red line is a fitted parabola to guide the eye.

N	z	$-\frac{L}{2\pi}\mathbf{k}_{\mathrm{T}}^{z}$	$\Omega_z/\Omega_{ m BZ}$	$rac{L}{2\pi}\mathbf{k}_{\mathrm{s}}^{z}$
33	0	(0,0,0)	1/100	(0.0813, 0.0500, 0.0250)
	1	(4, 1, 0)	1/75	(0.1464, 0.0552, 0.0250)
	2	(6, 3, 1)	13/840	(0.1972, 0.0757, 0.0332)
	3	(5, 5, 0)	11/600	(0.1712, 0.1362, 0.0250)
	4	(8, 3, 2)	25343/1345960	(0.2743, 0.0781, 0.0359)
	5	(7, 5, 3)	1787/29260	(0.2193, 0.1475, 0.0730)
	6	(10, 2, 0)	301/22770	(0.3483, 0.0460, 0.0122)
	7	(9, 5, 0)	1889/471960	(0.2917, 0.1500, 0.0073)
	8	(11, 3, 3)	549/32890	(0.3710, 0.0763, 0.0526)
	9	(10, 6, 3)	3734168/98423325	(0.3157, 0.1729, 0.0591)
	10	(8, 8, 5)	2/55	(0.2612, 0.2293, 0.1195)
	11	(9, 6, 6)	1007/24255	(0.2953, 0.1833, 0.1524)
	12	(12, 5, 1)	31/8073	(0.3750, 0.0972, 0.0110)
	13	(11, 7, 0)	1/600	(0.3246, 0.2217, 0.0050)
	14	(13, 6, 2)	27817/464100	(0.4036, 0.1435, 0.0467)
	15	(12, 7, 4)	347/36036	(0.3778, 0.1955, 0.1213)
	16	(11, 9, 3)	73/2100	(0.3364, 0.2701, 0.0601)
	17	(10, 9, 6)	65/1764	(0.3280, 0.2704, 0.1768)
	18	(11, 11, 0)	37/2520	(0.3578, 0.3237, 0.0187)
	19	(13, 8, 3)	2423/97240	(0.4171, 0.2540, 0.0893)
	20	(12, 8, 6)	199/24255	(0.3875, 0.2281, 0.1646)
	21	(11, 10, 5)	14593/556920	(0.3754, 0.3202, 0.1341)
	22	(13, 10, 2)	6613/245700	(0.4160, 0.3218, 0.0587)
	23	(15, 7, 1)	29/680	(0.4627, 0.1954, 0.0341)
	24	(15, 5, 5)	11/702	(0.4445, 0.1286, 0.1093)
	25	(11, 9, 9)	34/2205	(0.3324, 0.2836, 0.2479)
	26	(14, 9, 5)	9/11900	(0.4532, 0.3040, 0.1315)
	27	(12, 12, 4)	17/8190	(0.3904, 0.3712, 0.0948)
	28	(15, 9, 0)	13/840	(0.4605, 0.2957, 0.0250)
	29	(16, 6, 4)	16/663	(0.4786, 0.1662, 0.0926)
	30	(15, 7, 6)	97021/2702700	(0.4584, 0.2306, 0.1637)
	31	(13, 9, 8)	1027/29988	(0.4118, 0.2758, 0.2103)
	32	(14, 11, 4)	7/8398	(0.4516, 0.3239, 0.1226)
	33	(14, 13, 1)	1/189	(0.4327, 0.4082, 0.0172)
	34	(13, 13, 6)	15361/881790	(0.4234, 0.3905, 0.1528)
	35	(12, 11, 11)	2/315	(0.3532, 0.3171, 0.2813)
	36	(16, 12, 1)	1/75	(0.4774, 0.3750, 0.0274)
	37	(15, 13, 3)	8188/166725	(0.4644, 0.4082, 0.0853)
	38	(16, 10, 7)	13/2550	(0.4824, 0.2998, 0.1650)
	39	(14, 11, 10)	1/180	(0.4145, 0.3022, 0.2575)
	40	(16, 12, 6)	20/2907	(0.4821, 0.3647, 0.1430)
	41	(15, 12, 9)	79/2142	(0.4546, 0.3571, 0.1979)
	42	(14, 14, 12)	1/63	(0.4018, 0.3726, 0.2494)
	43	(16, 13, 12)	17/900	(0.4689, 0.3400, 0.2505)
	44	(16, 15, 15)	22/225	(0.4561, 0.4038, 0.3205)

Table S3. Index z, total momentum $\mathbf{k}_{\mathrm{T}}^z$, exact weight $\Omega_z/\Omega_{\mathrm{BZ}}$, and center $\mathbf{k}_{\mathrm{s}}^z$ of the IBZ regions for N=33.

N	$r_{\rm s}^2 K$	$r_{ m s}X$
7	1.77110059	-0.663751377
15	1.75971498	-0.630999714
19	1.75843687	-0.623184756
27	1.75774258	-0.613700247
33	1.75826227	-0.608535468
40	1.75615221	-0.605364222
57	1.75545710	-0.599501435
81	1.75453662	-0.595096762
93	1.75476609	-0.593397250
123	1.7545311(2)	-0.59069020(3)
147	1.7542302(2)	-0.58928659(4)
171	1.7544501(1)	-0.58801682(4)
179	1.7544764(2)	-0.58767775(4)
203	1.7541746(2)	-0.58696564(3)
251	1.7542188(1)	-0.58565017(4)
305	1.7541073(2)	-0.58465873(4)
515	1.7541090(1)	-0.58245938(5)
1021	1.7540160(2)	-0.58058038(5)
2007	1.7540110(2)	-0.57937257(5)
∞	1.75399969	-0.577252097

Table S4. Twist-averaged HF kinetic and exchange energies for the polarized UEG at several system sizes, in Ha. Energies for $N \leq 93$ are exact, and energies for $N \geq 123$ have been estimated using random sampling. The analytic $N \to \infty$ limit is also shown, for reference.

FITTING METHODOLOGY

In our work we use least-squares fits of energy data to perform extrapolations with respect to basis-set size and system size, as well as to handle parametrizations of the correlation energy. We avoid the use of "chi-square" fits in which each datum is weighed by the inverse of its squared uncertainty, since this distorts the relative importance of the data, in turn causing an underestimation of the uncertainty in functions of the fit. Instead we perform our least squares fits without these weights, and we obtain uncertainties by a stochastic process in which we replace each datum with a random number drawn from a normal distribution centred at its expected value of variance its standard error. The standard error in a function of the fit is then obtained as the square root of the variance of the values of the function in 10,000 realizations of this process.

We note that the statistical uncertainty in functions of the fit merely reflects that in the input data. The statistical uncertainty does not capture the bias due to the choice of a specific fitting function, which we refer to as *parametrization bias*, and has little practical meaning in the presence of large quasirandom fluctuations. We treat our energy data so that quasirandom fluctuations are almost negligible, and we use fitting functions with more parameters than strictly required for an

accurate fit in order to account for part of the parametrization bias. While this is not a rigorous approach, we expect our estimated statistical uncertainties to be at worst of the same order of magnitude as the true uncertainties.

VARIATIONAL AND DIFFUSION MONTE CARLO

The VMC method [S5, S6] requires a trial wave function Ψ_T to evaluate $\langle \Psi_T | \hat{H} | \Psi_T \rangle / \langle \Psi_T | \Psi_T \rangle$ by direct Monte Carlo integration in real space, and provides a framework for optimizing wave function parameters [S7, S8]. In the DMC method [S6, S9] the wave function is represented by a set of real-space walkers which evolves according to a small time-step approximation [S10] to the Green's function associated with the imaginary-time Schrödinger equation. The fixed node approximation prevents this process from collapsing onto the bosonic ground state by requiring the DMC wave function to have the same nodes as Ψ_T . The positive bias in the energy incurred by the fixed node approximation is referred to as the fixed node error, $\varepsilon_{\rm FN}$.

All of our VMC and DMC calculations have been performed using the CASINO code [S11]. Each of our DMC energies is obtained by linear extrapolation of the results of a DMC calculation consisting of M_1 steps with a time step of τ_1 and a target walker population of P_1 , and a second DMC calculation consisting of $M_2 = M_1/2$ steps with a time step of $\tau_2 = 4\tau_1$ and a target walker population of $P_2 = P_1/4$. We set $\tau_1 = 0.01r_{\rm s}^2$, $P_1 = 2048$ walkers, and adjust M_1 to obtain the desired statistical accuracy.

For our twist averaged VMC calculations we have used 6400 random values of \mathbf{k}_s , and for our twist averaged DMC calculations we have used up to 3200 values for the system sizes at which we compute the fixed node error, and 32 values for other system sizes.

Trial wave functions

The Slater-Jastrow form is a common choice of trial wave function for electronic systems, and consists of the HF determinant multiplied by a Jastrow correlation factor, $\Psi_{\rm T}({\bf R})=e^{J({\bf R})}\Psi_{\rm HF}({\bf R})$. We parametrize $J({\bf R})$ as [S12, S13]

$$J(\mathbf{R}) = \sum_{i < j} (1 - r_{ij}/L_u)^3 \Theta(r_{ij} - L_u) \sum_{l=0}^{8} \alpha_l r_{ij}^l$$

$$+ \sum_{i < j} \sum_{s=1}^{8} a_s \sum_{\mathbf{G} \in sth \ star} \cos(\mathbf{G} \cdot \mathbf{r}_{ij}) ,$$
(S9)

where Θ is the Heaviside step function, $\{\mathbf{G} \in s \text{th star}\}$ are the reciprocal lattice vectors of the simulation cell in the s th star of symmetry-equivalent vectors, and $\{\alpha_l\}$, $\{a_s\}$ and L_u are optimizable parameters. Note that we impose the parallel-spin Kato cusp condition [S14] by setting $\alpha_0 = (\alpha_1 - 1/4)L_u/3$.

In our multideterminantal benchmark of FCIQMC we replace the HF determinant with a selected-CI expansion extracted from FCIQMC.

Backflow transformations [S15–S19] offer the ability to modify the nodes of the Slater-Jastrow wave function and give significantly lower DMC energies. Backflow transformations replace the argument ${\bf R}$ of the Slater determinants with transformed coordinates ${\bf X}({\bf R})$ which we parametrize as [S19]

$$\mathbf{x}_{i} = \mathbf{r}_{i} + \sum_{j \neq i} (1 - r_{ij}/L_{\eta})^{3} \Theta(r_{ij} - L_{\eta}) \sum_{l=0}^{8} c_{l} r_{ij}^{l} \mathbf{r}_{ij} ,$$
(S10)

where $\{c_l\}$ and L_{η} are optimizable parameters. Note that we set $c_0 = c_1 L_{\eta}/3$ to avoid interfering with the parallel-spin Kato cusp condition.

FULL CONFIGURATION-INTERACTION QUANTUM MONTE CARLO

The FCIQMC method [S20–S23] obtains the CI coefficients by evolution of a population of random walkers, each associated with a determinant in Hilbert space, in imaginary time via diagonal death/cloning and off-diagonal spawning processes. An annihilation step is carried out at each time step to cancel walkers of opposite signs on the same determinant, which is crucial for sign coherence [S20]. The initial set of walkers, 100 in our calculations, is usually placed on the HF determinant, and after an equilibration stage the occupation of each determinant is on average proportional to its exact CI coefficient.

The initiator approximation modifies the dynamics of the random walk so that spawning new walkers on unpopulated determinants from sites that contain less than $n_{\rm init}$ walkers is forbidden, where $n_{\rm init}$ is a tunable parameter which we set to 3 in our calculations. This allows a substantial reduction in the number of walkers W required for convergence, but is a source of bias [S21–S23]. The initiator error vanishes as $W \to \infty$, and in practice we increase the walker population until energy changes become negligible. Our largest calculations use up to $W=1.5\times10^8$ walkers. The number of walkers required to overcome the initiator error increases with the size of the Hilbert space of the system, which grows very quickly with system size, and has also been observed to increase with $r_{\rm s}$ [S24, S25].

Figure S3 represents the equilibrated walker population on the leading determinants of the CI wave function for one of the systems reported in our work.

Basis-set extrapolation

Basis sets for the UEG consist of the M plane waves with the smallest wave vectors. This finite basis set provides access to a finite portion of the Hilbert space of the system, resulting in a positive energy bias. The infinite basis set limit can be

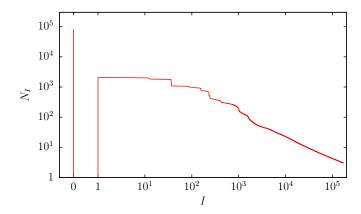


Figure S3. Walker population N_I on Slater determinant D_I as a function of I, sorted by decreasing N_I , for the 19-electron gas at $r_{\rm s}=1$ and ${\bf k}_{\rm s}={\bf 0}$ using a 341-plane-wave basis and 10^7 walkers. The first peak corresponds to the HF determinant.

estimated by extrapolation, as is standard practice in quantum chemistry [S26]. We extrapolate our FCIQMC correlation energies at each IBZ region z to the complete basis set limit using the fitting function

$$E_{\text{corr}}^z(M) = E_{\text{corr}}^z(\infty) + a_z M^{-1} + b_z M^{-2}$$
, (S11)

where $E_{\rm corr}^z(\infty)$, a_z , and b_z are fit parameters. Setting $a_z=0$ yields a very good fit to the energy data, but we keep a_z as a fit parameter to account for the parametrization bias.

We find that the basis-set error is roughly independent of z, as shown in Fig. S4 for the 19-electron gas at $r_{\rm s}=1$. To reduce the cost of our FCIQMC calculations for selected systems ($N=19,\,27,\,{\rm and}\,33$ at $r_{\rm s}=0.5$) we perform the basis set extrapolation in the Γ -point region, $z=0,\,{\rm only}.$ For other regions we evaluate the correlation energy at a single basis set size $M~(\simeq~1050,\,830,\,{\rm and}~830,\,{\rm respectively})$ and we obtain $E_{\rm corr}^z(\infty)$ from Eq. S11 by setting $a_z=a_0$ and $b_z=b_0$.

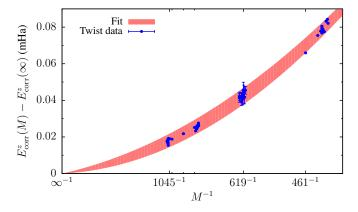


Figure S4. Finite basis set error in the FCIQMC correlation energy as a function of inverse basis-set size M^{-1} for the 19-electron gas at $r_{\rm s}=1$. The data correspond to calculations at multiple basis-set sizes in each of the 13 IBZ regions.

We investigate the bias incurred by this approximation by comparing the value of b_0 with its average $b_{\rm ave} = \sum_z \left(\Omega_z/\Omega_{\rm BZ}\right) b_z$ in fits of our data at $r_{\rm s}=1$ to Eq. S11 with $a_z=0$. The largest deviation occurs for the 27-electron gas, for which $|1-b_0/b_{\rm ave}|=0.153$. Therefore a contribution of $0.153 \times b_0 M^{-2}$ is added (in quadrature) to the uncertainty of the twist-averaged energy for the systems for which we use the Γ -point extrapolation scheme, which we expect to overestimate the corresponding bias. This correction represents an increase in the uncertainty of the twist-averaged correlation energy by up to 75%, but despite this, the Γ -point extrapolation method provides a net reduction in the computational cost of the FCIQMC calculations.

FINITE SIZE ERRORS

Finite system results and extrapolation

In Table S5 we give the full set of twist-averaged DMC correlation energies obtained in our work, and Table S6 shows the FCIQMC results. For completeness, we also give total-energy versions of these data in Tables S7 and S8. We plot our DMC and FCIQMC correlation energies in Fig. S5, along with the corresponding fits.

		$E_{ m corr}^{ m FN}$	
N	$r_{\rm s} = 0.5$	$r_{\rm s} = 1.0$	$r_{\rm s} = 5.0$
15	-12.883(6)	-12.144(3)	
19	-14.636(10)	-13.665(8)	-9.425(6)
27	-16.953(9)	-15.654(9)	
33	-18.455(9)	-17.009(34)	-10.943(6)
40	-19.526(94)	-17.683(30)	
57	-21.757(64)	-19.549(47)	-12.017(6)
81	-23.750(36)	-21.065(22)	
93	-24.598(9)	-21.709(14)	-12.779(4)
123	-26.108(33)	-22.769(17)	
147	-26.984(20)	-23.373(33)	-13.344(4)
171	-27.762(11)	-23.956(7)	
179	-27.981(12)	-24.135(15)	
203	-28.493(15)	-24.463(11)	-13.677(3)
251	-29.487(14)	-25.099(18)	-13.872(6)
305	-30.294(13)	-25.660(7)	-14.021(2)
515	-32.204(6)	-26.892(2)	-14.3616(5)
1021		-28.085(3)	
∞	-38.778(10)	-30.650(3)	-15.270(4)

Table S5. Twist-averaged DMC correlation energies of the polarized UEG at $r_{\rm s}=0.5,\,1,$ and 5 and their respective thermodynamic limits, in mHa.

To illustrate the magnitude of the quasirandom fluctuations in the DMC energy as a function of N, in Fig. S6 we plot the fit error for the Γ -point DMC energy, the twist-averaged HF

	$r_{\rm s}=0.5$		$r_{\rm s} = 1.0$	
N	$E_{\rm corr}$	$arepsilon_{ ext{FN}}$	$E_{\rm corr}$	$\varepsilon_{\mathrm{FN}}$
15	-13.5203(7)	0.638(6)	-12.6926(4)	0.549(3)
19	-15.404(3)	0.769(10)	-14.313(4)	0.648(9)
27	-17.918(7)	0.965(12)	-16.395(1)	0.741(9)
33	-19.516(13)	1.061(15)		
∞	-40.44(5)	1.67(5)	-31.70(4)	1.05(4)

Table S6. Exact (FCIQMC) correlation energies and fixed node error for the polarized UEG at $r_{\rm s}=0.5$ and 1 for different system sizes and their respective thermodynamic limits, in mHa.

		$E_{ m tot}^{ m FN}$	
N	$r_{\rm s} = 0.5$	$r_{\rm s} = 1.0$	$r_{\rm s} = 5.0$
15	5.763978(6)	1.116571(3)	
19	5.772742(10)	1.121587(8)	-0.063725(6)
27	5.786617(9)	1.128388(9)	· /
33	5.797524(86)	1.132718(34)	-0.062320(6)
40	5.794355(94)	1.133105(30)	
57	5.801068(64)	1.136407(47)	-0.061699(6)
81	5.804203(36)	1.138375(22)	
93	5.807672(9)	1.139660(14)	-0.061268(4)
123	5.810636(33)	1.141072(17)	
147	5.811364(20)	1.141570(33)	-0.061032(4)
171	5.814004(12)	1.142477(7)	
179	5.814569(12)	1.142664(15)	
203	5.814274(15)	1.142746(11)	-0.060903(3)
251	5.816088(14)	1.143470(18)	-0.060833(6)
305	5.816817(13)	1.143789(7)	-0.060788(2)
515	5.819314(6)	1.144758(2)	-0.0606891(5)
1021		1.145350(3)	
∞	5.822717(10)	1.146098(3)	-0.060560(4)

Table S7. Twist-averaged DMC total energies of the polarized UEG at $r_{\rm s}=0.5,\,1,$ and 5 and their respective thermodynamic limits, in Ha.

	$E_{ m tot}$		
N	$r_{\rm s} = 0.5$	$r_{\rm s} = 1.0$	
15	5.7633402(7)	1.1160227(4)	
19	5.7719736(26)	1.1209393(39)	
27	5.7856521(72)	1.1276472(14)	
33	5.7964623(129)		
∞	5.82105(5)	1.14505(4)	

Table S8. Exact (FCIQMC) total energies for the polarized UEG at $r_{\rm s}=0.5$ and 1 for different system sizes and their respective thermodynamic limits, in Ha.

energy, and the twist-averaged DMC energy with and without

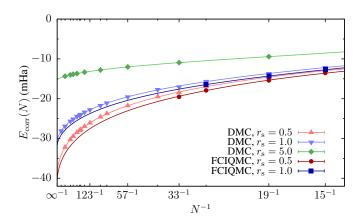


Figure S5. Full set of twist-averaged DMC and FCIQMC correlation energies as a function of inverse system size, along with finite-size extrapolation fits described in the manuscript. The uncertainty in the fitted curves is smaller than the line width.

the ΔK and ΔX corrections at $r_{\rm s}=0.5$. For the Γ -point DMC energy we have used a fitting function consisting of a single N^{-1} term, while in the other cases we have used fitting functions containing up to N^{-2} , as in Eq. 1 of our manuscript. These fit errors are expected to be proportional to N^{-1} , and in Fig. S6 we plot straight lines of this form to guide the eye.

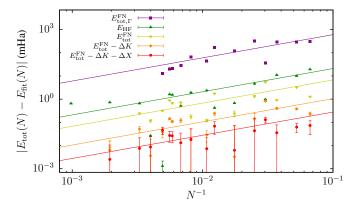


Figure S6. Absolute fit error as a function of N^{-1} for the HF and fixed node DMC energy at $r_{\rm s}=0.5$ with various corrections. The lines are functions proportional to N^{-1} , intended as a guide to the eye.

At this density, twist-averaging reduces the magnitude of the quasirandom fluctuations by two orders of magnitude. The ΔK correction affords a further reduction by a factor of 7, while ΔX achieves an additional factor of 4. We note that the fit errors in $E_{\rm tot}^{\rm FN}-\Delta K-\Delta X$ are of the order of the uncertainty to which we have evaluated the DMC energies.

Evaluation of integration errors at k = 0

As shown in Refs. S3 and S27, some of the leading-order finite-size errors in DMC energies can be ascribed to integration errors which are effectively due to the inability to sample $\mathbf{k} = \mathbf{0}$ at finite N. We define the object

$$\epsilon_n(\alpha) = \Omega^{\frac{n+1}{3}} \left[(2\pi)^{-3} \int \frac{4\pi}{k^2} k^n e^{-\alpha k^2} \, d\mathbf{k} - \frac{1}{\Omega} \sum_{\mathbf{G} \neq \mathbf{0}} \frac{4\pi}{G^2} G^n e^{-\alpha G^2} \right], \tag{S12}$$

where Ω is the simulation cell volume, whose limit $\epsilon_n = \lim_{\alpha \to 0} \epsilon_n(\alpha)$ represents the error in the discretization of the reciprocal-space convolution of the interaction potential $\frac{4\pi}{k^2}$ and a power of the wave vector k^n .

The finite size error in the HF exchange energy of the polarized UEG due to integrations errors at $\mathbf{k} = \mathbf{0}$ (given in Eq. 41 of Ref. S3 for the unpolarized UEG) can be written in terms of ϵ_n as

$$X(N) = X(\infty) - \frac{3\epsilon_1}{16\pi} r_{\rm s}^{-1} N^{-2/3} + \frac{\epsilon_3}{(4\pi)^3} \left(\frac{\pi}{6}\right)^{2/3} r_{\rm s}^{-1} N^{-4/3} + \dots$$
(S13)

Note that, in the notation of Ref. S3, $\epsilon_1 = 2C_{\rm HF}$. The finite size error in the DMC kinetic energy of the polarized UEG due to integration errors at ${\bf k}={\bf 0}$ (given in Eq. 56 of Ref. S3) can also be expressed in terms of ϵ_n ,

$$T(N) = T(\infty) - \frac{\sqrt{3}}{4} r_{\rm s}^{-3/2} N^{-1} + \frac{\epsilon_3}{16\pi} r_{\rm s}^{-2} N^{-4/3} + \dots$$
 (S14)

Note that, in the notation of Ref. S3, $\epsilon_3 = 4C_{3D}$.

By manipulating Eq. S12 we arrive at a computable expression for $\epsilon_n(\alpha)$,

$$\epsilon_n(\alpha) = \Omega^{\frac{n+1}{3}} \left[\frac{\Gamma\left(\frac{n+1}{2}\right)}{\pi \alpha^{\frac{n+1}{2}}} - \frac{4\pi}{\Omega} \sum_{\mathbf{G} \neq \mathbf{0}} G^{n-2} e^{-\alpha G^2} \right], \tag{S15}$$

where Γ is the Gamma function. The numerical evaluation of ϵ_n requires computing $\epsilon_n(\alpha)$ at increasingly small values of α until a convergence criterion is met. As can be gathered from Eq. S15, $\epsilon_n(\alpha)$ at $\alpha \to 0$ is the difference of increasingly large numbers, one of which is itself an infinite sum which needs to be converged independently. This is numerically delicate, and we find that rounding errors prevent obtaining more than 4–5 decimal places of precision in the value of ϵ_n with this procedure.

However, inspection of the behavior of $\epsilon_n(\alpha)$ with α reveals an exponential convergence pattern, which can be exploited to produce much more accurate estimates of ϵ_n at values of α at

which rounding errors are not problematic. Using the model $\epsilon_n(\alpha) = \epsilon_n e^{-p_1 \alpha}$ we find a two-point extrapolation formula,

$$\epsilon_n \approx \epsilon_n^2(\alpha)\epsilon_n^{-1}(2\alpha)$$
, (S16)

a higher-order model $\epsilon_n(\alpha) = \epsilon_n e^{-p_1 \alpha - p_2 \alpha^2}$ yields a three-point extrapolation formula,

$$\epsilon_n \approx \epsilon_n^{8/3}(\alpha)\epsilon_n^{-2}(2\alpha)\epsilon_n^{1/3}(4\alpha) ,$$
(S17)

and a three-parameter model $\epsilon_n(\alpha) = \epsilon_n e^{-p_1 \alpha - p_2 \alpha^2 - p_3 \alpha^3}$ results in a four-point extrapolation formula,

$$\epsilon_n \approx \epsilon_n^{64/21}(\alpha)\epsilon_n^{-8/3}(2\alpha)\epsilon_n^{2/3}(4\alpha)\epsilon_n^{-1/21}(8\alpha)$$
, (S18)

We plot the values of $\epsilon_3(\alpha)$ and the results from the three extrapolation formulae in Fig. S7. This technique significantly accelerates convergence: Eq. S18 gives ϵ_3 to 14-digit precision at a value of α at which $\epsilon_3(\alpha)$ is only accurate to 4 decimal places. We note that we have used 128-bit floating-point

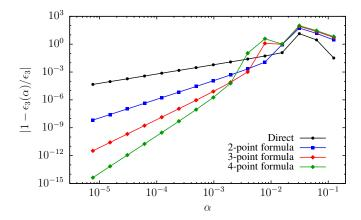


Figure S7. Convergence of the integration error $\epsilon_3(\alpha)$ as a function of α , along with extrapolated estimates from the two-point formula of Eq. S16 and the three-point formula of Eq. S17.

arithmetic ("quad" precision) to further enhance numerics. With this approach we obtain the values $\epsilon_1 = 5.674594959$ and $\epsilon_3 = 21.04959845$ for our simple cubic simulation cell.

Other sources of finite-size errors

Besides integration errors and quasirandom fluctuations, there is a third source of finite-size errors in twist-averaged energies. As reported in Table I of Ref. S2, the twist-averaged HF kinetic energy exhibits finite-size errors that scale as $N^{-4/3}$ to leading order. These finite size errors arise due to the use of the canonical ensemble, *i.e.*, keeping N fixed as $\mathbf{k}_{\rm s}$ is varied during twist-averaging, and is associated with the mismatch between the Fermi wave vector at size N and in the thermodynamic limit [S2]. In other words, these are integration errors at $k = k_{\rm F}$ due to the smearing of the Fermi surface as an artifact of twist-averaging in the canonical ensemble.

We observe in our data that the estimate of the finite-size error at order $N^{-4/3}$ in the HF exchange energy given by Eq. S13 and in the DMC kinetic energy given by Eq. S14 do not completely account for the finite-size error at order $N^{-4/3}$ in either of these energy components or in the DMC correlation energy. We hypothesize that integration errors at $k=k_{\rm F}$ from the various energy components enter the DMC correlation energy at order $N^{-4/3}$ and would need to be fully accounted for in order to determine the c_4 coefficient in Eq. 1 of our manuscript. For this reason we treat all coefficients beyond order N^{-1} as fit parameters in our analysis of the correlation energies.

Our DMC correlation energies are well described by Eq. 1 of our manuscript with $c_6=0$, but we keep c_6 as a fit parameter to account for the parametrization error.

ADDITIONAL RESULTS

Accuracy of the ξ -scale extrapolation

In our manuscript we find that correlation energies at high densities are accurately described by polynomials in $\xi=r_{\rm s}^{-3/2}N^{-1}$ with density-independent coefficients. The fit shown in Fig. 4 of our manuscript yields fixed node correlation energies in the thermodynamic limit of -38.722(8) and -30.658(2) mHa at $r_{\rm s}=0.5$ and 1, respectively, which differ by 4.3 and 2.0 standard deviations from the values obtained by independent extrapolation at each density given in Table S5.

Modified PW92 parameters

In our manuscript we present values of the correlation energy from alternative fits to the PW92 form for the correlation energy of the polarized UEG [S28]. In particular, we introduce an unweighted fit to the CA data [S29] (uPW92) and a revised unweighted fit to the CA data and our results (rPW92). In Table S9 we provide the parameter values that reproduce the mean values of the various fits.

The parameters in the uPW92 and rPW92 fits have very similar values, and, while this might well be coincidental, it is of potential interest to report the equivalent uPW92 fit for the unpolarized UEG, which we have not considered in our work. In Table S10 we provide the parameter values that reproduce the mean values of the unweighted PW92 fit to the CA data for the unpolarized UEG.

	α_1	β_3	eta_4
PW92	0.20548	3.3662	0.62317
PW92*	0.202326	3.30573	0.615932
uPW92	0.264193	4.78287	0.750424
rPW92	0.266529	4.86059	0.750188

Table S9. Values of the free parameters in the PW92 parametrization of the correlation energy of the polarized UEG, named α_1 , β_3 , and β_4 following the notation of Ref. S28. Listed are the values given in Ref. S28 (PW92), the similar values we obtain with a weighted fit to the CA data using our fitting methodology (PW92*), the values we obtain with an unweighted fit to the CA data (uPW92), and the values we obtain with an unweighted fit to the CA data and our present results (rPW92).

	α_1	β_3	eta_4
PW92	0.21370	1.6382	0.49294
PW92*	0.216518	1.66722	0.498875
uPW92	0.227012	1.76522	0.523918

Table S10. Values of the free parameters in the PW92 parametrization of the correlation energy of the unpolarized UEG, named α_1 , β_3 , and β_4 following the notation of Ref. S28. Listed are the values given in Ref. S28 (PW92), the similar values we obtain with a weighted fit to the CA data using our fitting methodology (PW92*), and the values we obtain with an unweighted fit to the CA data (uPW92).

- [S1] P. P. Ewald, Die Berechnung optischer und elektrostatischer Gitterpotentiale, Ann. Phys. 64, 253 (1921).
- [S2] C. Lin, F. H. Zong, and D. M. Ceperley, Twist-averaged boundary conditions in continuum quantum Monte Carlo algorithms, Phys. Rev. E 64, 016702 (2001).
- [S3] N. D. Drummond, R. J. Needs, A. Sorouri, and W. M. C. Foulkes, *Finite-size errors in continuum quantum Monte Carlo calculations*, Phys. Rev. B 78, 125106 (2008).
- [S4] J. J. Shepherd, A quantum chemical perspective on the homogeneous electron gas, PhD thesis, University of Cambridge (2013).
- [S5] W. L. McMillan, Ground State of Liquid He⁴, Phys. Rev. 138, A442 (1965).
- [S6] W. M. C. Foulkes, L. Mitas, R. J. Needs, and G. Rajagopal, *Quantum Monte Carlo simulations of solids*, Rev. Mod. Phys. 73, 33 (2001).
- [S7] J. Toulouse and C. J. Umrigar, Optimization of quantum Monte Carlo wave functions by energy minimization, J. Chem. Phys. 126, 084102 (2007).
- [S8] C. J. Umrigar, J. Toulouse, C. Filippi, S. Sorella, and R. G. Hennig, Alleviation of the Fermion-Sign Problem by Optimization of Many-Body Wave Functions, Phys. Rev. Lett. 98, 110201 (2007).
- [S9] J. B. Anderson, *Quantum chemistry by random walk*. $H^{-2}P$, H_3^+ $D_{3h}^{-1}A_1'$, $H_2^ 3\Sigma_u^+$, $H_4^{-1}\Sigma_g^+$, $Be^{-1}S$, J. Chem. Phys. **65**, 4121 (1976).
- [S10] A. Zen, S. Sorella, M. J. Gillan, A. Michaelides, and D. Alfè, *Boosting the accuracy and speed of*

- quantum Monte Carlo: Size consistency and time step, Phys. Rev. B **93**, 241118(R) (2016).
- [S11] R. J. Needs, M. D. Towler, N. D. Drummond, and P. López Ríos, Continuum variational and diffusion quantum Monte Carlo calculations, J. Phys.: Condens. Matter 22, 023201 (2010).
- [S12] N. D. Drummond, M. D. Towler, and R. J. Needs, Jastrow correlation factor for atoms, molecules, and solids, Phys. Rev. B 70, 235119 (2004).
- [S13] P. López Ríos, P. Seth, N. D. Drummond, and R. J. Needs, Framework for constructing generic Jastrow correlation factors, Phys. Rev. E 86, 036703 (2012).
- [S14] T. Kato, On the eigenfunctions of manyparticle systems in quantum mechanics, Comm. Pure Appl. Math. 10, 151 (1957).
- [S15] V. R. Pandharipande and N. Itoh, Effective Mass of ³He in Liquid ⁴He, Phys. Rev. A 8, 2564 (1973).
- [S16] K. E. Schmidt and V. R. Pandharipande, New variational wave function for liquid ³He, Phys. Rev. B 19, 2504 (1979).
- [S17] Y. Kwon, D. M. Ceperley, and R. M. Martin, Effects of backflow correlation in the three-dimensional electron gas: Quantum Monte Carlo study, Phys. Rev. B 58, 6800 (1998).
- [S18] M. Holzmann, D. M. Ceperley, C. Pierleoni, and K. Esler, Backflow correlations for the electron gas and metallic hydrogen, Phys. Rev. E 68, 046707 (2003).
- [S19] P. López Ríos, A. Ma, N. D. Drummond, M. D. Towler, and R. J. Needs, *Inhomogeneous backflow transformations in quantum Monte Carlo calculations*, Phys. Rev. E 74, 066701 (2006).
- [S20] G. H. Booth, A. J. W. Thom, and A. Alavi, Fermion Monte Carlo without fixed nodes: A game of life,

- death, and annihilation in Slater determinant space, J. Chem. Phys. 131, 054106 (2009).
- [S21] D. Cleland, G. H. Booth, and A. Alavi, Survival of the fittest: Accelerating convergence in full configuration-interaction quantum Monte Carlo, J. Chem. Phys. 132, 041103 (2010).
- [S22] D. Cleland, G. H. Booth, and A. Alavi, A study of electron affinities using the initiator approach to full configuration interaction quantum Monte Carlo, J. Chem. Phys. 134, 024112 (2011).
- [S23] G. H. Booth, D. Cleland, A. J. W. Thom, and A. Alavi, Breaking the carbon dimer: The challenges of multiple bond dissociation with full configuration interaction quantum Monte Carlo methods, J. Chem. Phys. 135, 084104 (2011).
- [S24] J. J. Shepherd, G. H. Booth, and A. Alavi, Investigation of the full configuration interaction quantum Monte Carlo method using homogeneous electron gas models, J. Chem. Phys. 136, 244101 (2012).
- [S25] J. J. Shepherd, G. H. Booth, A. Grüneis, and A. Alavi, Full configuration interaction perspective on the homogeneous electron gas, Phys. Rev. B 85, 081103(R) (2012).
- [S26] T. Helgaker, P. Jørgensen, and J. Olsen, Molecular Electronic-Structure Theory (Wiley, Chichester, 2000).
- [S27] S. Chiesa, D. M. Ceperley, R. M. Martin, and M. Holzmann, Finite-Size Error in Many-Body Simulations with Long-Range Interactions, Phys. Rev. Lett. 97, 076404 (2006).
- [S28] J. P. Perdew, Y. Wang, Accurate and simple analytic representation of the electron-gas correlation energy, Phys. Rev. B 45, 13244 (1992).
- [S29] D. M. Ceperley and B. J. Alder, Ground State of the Electron Gas by a Stochastic Method, Phys. Rev. Lett. 45, 566 (1980).